Journal of Zhejiang University-SCIENCE A 2026 27(5):518-533
www.jzus.zju.edu.cn; www.springer.com/journal/11582
E-mail: jzus_a@zju.edu.cn

Research Article
https://doi.org/10.1631/jzus.A2500407

Effect of tamping duration on mechanical properties of ballast beds: a DEM–MBD coupled investigation

Chao KONG[1], Tao XIN[1,2]✉, Zhongxia QIAN[1], Yi YANG[1], Chuanqing DAI[1], Yanhua LI[1], Sen WANG[3,4]

[1]*School of Civil Engineering, Beijing Jiaotong University, Beijing 100044, China*
[2]*Beijing Key Laboratory of Track Engineering, Beijing 100044, China*
[3]*Railway Engineering Research Institute, China Academy of Railway Sciences Co., Ltd., Beijing 100081, China*
[4]*State Key Laboratory of High Speed Railway Track System, Beijing 100081, China*

Abstract: As a critical maintenance method for ballasted tracks, tamping operations effectively improve ballast bed compactness and mechanical performance. Tamping duration critically influences the mechanical response of the ballast bed, yet systematic studies on the relationship between the duration of tamping and the mechanical performance of ballasted tracks are lacking. In this study, we established a discrete element method–multibody dynamics (DEM–MBD) coupled model of tamping machinery and a ballasted track to systematically analyze the effects of tamping duration on ballast bed compactness, particle motion, and ballast contact behavior. The results show that increasing the tamping duration enhances the compactness beneath sleepers and the uniformity of compactness in the ballast bed. Tamping duration significantly affects ballast motion. A prolonged tamping duration significantly decelerates ballast particle movement beneath sleepers, particularly during the inserting stage, while in the squeezing stage, it exhibits a smaller decrease. The inter-sleeper region is particularly sensitive to tamping duration variation, showing substantial velocity reductions in ballast particles during both the inserting and lifting stages. Increased tamping duration rapidly decreases contact forces in ballast particles during the inserting stage, stabilizes contact forces in the squeezing stage, and elevates the coordination number among ballast particles. The squeezing stage exhibits the most significant mechanical energy fluctuations, while the evolution patterns of translational and rotational kinetic energies show strong correlations with ballast motion characteristics. Appropriately increasing the tamping duration enhances the overall mechanical performance of the ballast bed and extends track maintenance cycles. This study revealed the mechanism underlying the effects of tamping duration on the mechanical behavior of ballast beds, providing a theoretical foundation for the precise design of tamping parameters.

Key words: Tamping operation; Ballasted track; Tamping duration; Discrete element model (DEM); Contact force

1 Introduction

A ballasted track structure, one of the most widely used railway configurations globally, is characterized by ease of construction, low cost, and convenient maintenance (Indraratna, 2016; Zhang et al., 2019). Its components include rails, fastening systems, sleepers, and a ballast bed. The ballast bed, composed of granular particles beneath sleepers, serves as a critical structural element for supporting train-induced loads and ensures the safe and stable operation of railway lines.

Long-term train operations lead to inevitable degradation of the track geometry, inducing settlement and deformation defects in ballasted track structures that compromise operational safety (Gu et al., 2022; Qian et al., 2022; Cui et al., 2024). Regular maintenance is critical to mitigate these issues. Large tamping vehicles are now widely adopted as an effective maintenance approach (Fig. S1 of the electronic supplementary materials (ESM)). Tamping units compact ballast beneath sleepers along both rail sides during the squeezing stage, enhancing compactness to mitigate geometric irregularities such as vertical alignment and improve track quality (Guo et al., 2021).

Recent studies have focused on field and laboratory investigations into the operational mechanisms and dynamic responses of tamping processes. Barbir et al. (2018) developed a monitoring system for tamping

---

✉ Tao XIN, xint@bjtu.edu.cn
Tao XIN, https://orcid.org/0000-0002-4283-0913

Received Aug. 28, 2025; Revision accepted Nov. 1, 2025; Crosschecked Jan. 22, 2026; Online first Apr. 14, 2026

© Zhejiang University Press 2026

operations, analyzing compaction efficiency across various ballast bed configurations. Kumara and Hayano (2016) used scaled-down experiments and particle image velocimetry to quantify deformation patterns induced by tamping. Offenbacher et al. (2021) proposed integrating sensors into tamping devices to evaluate ballast conditions through systematic data acquisition. Abbasi et al. (2024) revealed via field measurements that tamping reduces the rail support modulus by 75.5%, while subsequent stabilization increases it by 35.8%. Liu et al. (2020) analyzed variations in the stiffness and damping of ballast beds under different numbers of tamping operations using impact excitation techniques while investigating vibration transmission characteristics. Aingaran et al. (2018) showed through triaxial tests that stress reversal disrupts the load-bearing structure of ballast, with tamping impairing its elastic resistance to cyclic vertical loads. Using smart ballast, a ballast bed condition monitoring device that simulates the physical characteristics of real ballast, Zhou et al. (2024) collected acceleration and stress data during tamping operations to compare the effects of squeezing duration and frequency. Wang et al. (2022) used smart ballast to analyze triaxial acceleration data and power spectra in mud pumping sections of heavy haul lines during maintenance, validating its feasibility for monitoring ballast bed conditions. Zhang et al. (2024) conducted field experiments on the vibration transmission and attenuation characteristics of ballasted tracks during tamping, emphasizing the effects of the number of tamping operations and recommending that there should be no more than three. Xiao et al. (2023) experimentally assessed tamping and stabilization practices for newly constructed lines, discussing critical parameters including tamping modes, stabilization frequencies, and track lifting heights.

In a simulation analysis of tamping operations, Przybyłowicz et al. (2022) compared vertical and side tamping techniques through scaled experiments and discrete element analysis, showing that side tamping technology increased residual stresses beneath sleepers fivefold and exhibited superior long-term anti-settlement performance. Zhou et al. (2013) established a numerical model to analyze ballast movement trends, concluding that 35 Hz represents the optimal vibration frequency. Shi et al. (2020) developed a discrete element method–multibody dynamics (DEM–MBD) coupling model based on the DCL-32 tamping machine for simultaneous tamping of two sleepers, analyzing the compaction, contact forces, and support stiffness of the ballast bed. They recommended operational parameters of 20 mm lifting height, 35 Hz vibration frequency, and 20 mm tamping depth. Gao et al. (2023) developed an apparatus for measuring impact forces during tamping and established an expression for evaluating ballast bed mechanical properties based on impact forces, enabling real-time assessment. Shi et al. (2021) constructed a tamping device–ballast bed model to analyze particle breakage during tamping and proposed recommendations for particle gradation. Zhang et al. (2023b) established a three-sleeper tamping device–ballast bed model using polyhedral particles and virtual units, investigating the effect of squeezing force on ballast bed mechanical performance and recommending a squeezing force of 7.8 kN. They also conducted a detailed analysis of the patterns of evolution of the degree of compaction and contact forces in different regions of the ballast bed during tamping (Zhang et al., 2023a). For tamping research in turnout areas, Chi et al. (2022) established a tamping device–ballast bed analysis model to evaluate the operational efficacy of the CDC-16 tamping machine. They analyzed the effects of tamping tine vibration frequency and amplitude and derived optimal operational parameters using response surface methodology (Chi et al., 2024a). Shi et al. (2024) developed an intelligent optimization method for tamping parameters based on a discrete element method and radial basis function–multi-objective genetic algorithm (DEM–RBF–MOGA), revealing interaction mechanisms among operational parameters and proposing optimal solutions. Gao et al. (2024) combined field experiments and simulations to investigate the effect of tamping frequency on ballast bed dynamic behavior, showing that frequencies of 30–40 Hz yield the best maintenance outcomes.

In summary, as shown in the literature and the compilation of typical research dimensions for tamping operations (Table S1 of the ESM), although field tests partially consider the effect of time parameters, they fail to fully analyze meso-mechanical mechanisms. Numerical simulations generally fix the tamping duration, neglecting its essential impact on mechanical characteristics of the ballast bed. Parameter optimization studies also do not incorporate duration into the variable space. Thus, the mechanistic effect of time parameters on ballast bed structural performance throughout a complete tamping process has not been sufficiently investigated, representing a critical research gap. In this study, we established a DEM–MBD coupling model of the tamping device–ballast bed system to investigate the relationship between the tamping duration and meso-dynamic responses of the ballast bed. The research aimed to uncover the mechanisms influencing tamping duration and provide theoretical guidance for ballasted track maintenance. The co-simulation workflow for the tamping device–ballast bed system is shown in Fig. S2 of the ESM.

2 Simulation analysis model

2.1 Ballast particle simulation and ballast bed construction

The ballast bed is the critical structural layer of ballasted track systems, functioning as the foundational support for the track framework. This layer mainly transfers vertical loads from sleepers to the subgrade, maintains the geometric stability of the track, and provides necessary elastic damping. The angular and irregular morphology of ballast particles may lead to variability in the macroscopic mechanical responses of the ballast bed (Xu et al., 2021; Aela et al., 2022). The 3D laser scanning technology, following the methodology of Shi et al. (2020), enabled accurate reconstruction of surface geometric features through 3D scans of 12 representative ballast samples, resolving challenges in characterizing particle morphology. The methodology of Lim and McDowell (2005) was used to establish a high precision multi-sphere cluster model on a discrete element simulation platform (Fig. 1), effectively addressing the accurate representation of irregular particle morphology and ensuring the reliability of DEM analysis results.

Following the railway ballast standard (TB/T 2140-2008) (MOR, 2008), the ballast bed model was constructed using the special-grade ballast gradation control curve (Fig. 2). The cross-sectional parameters were selected according to the railway track design standard (TB 10082-2017) (NRA, 2017) and included a layer thickness of 350 mm, shoulder width of 500 mm, and slope ratio of 1.00:1.75. Sleepers were imported as geometric entities and arranged at equal intervals of 600 mm.

To investigate the mechanism of the dynamic interaction between tamping devices and the ballast bed while considering boundary condition effects, a numerical model with a four-sleeper-length ballast bed section was established. Spatial randomness of ballast particles was achieved through gravity-driven random placement in discrete element modeling combined with a multi-stage compaction process to regulate ballast bed compactness, ultimately establishing a ballast bed simulation model that complied with railway industry technical specifications (Fig. 3).

2.2 Tamping device–ballasted track coupling model

We used a commonly used tamping device to obtain actual geometric dimensions (Fig. 4) and then established a geometric model of the tamping machinery. The complete operational sequence of a tamping device includes sleeper elevation, tamper inserting stage, squeezing stage, tamper reverse rotation, and tamp lifting stage. The geometric motion behavior of both the tamping device and sleepers was simulated

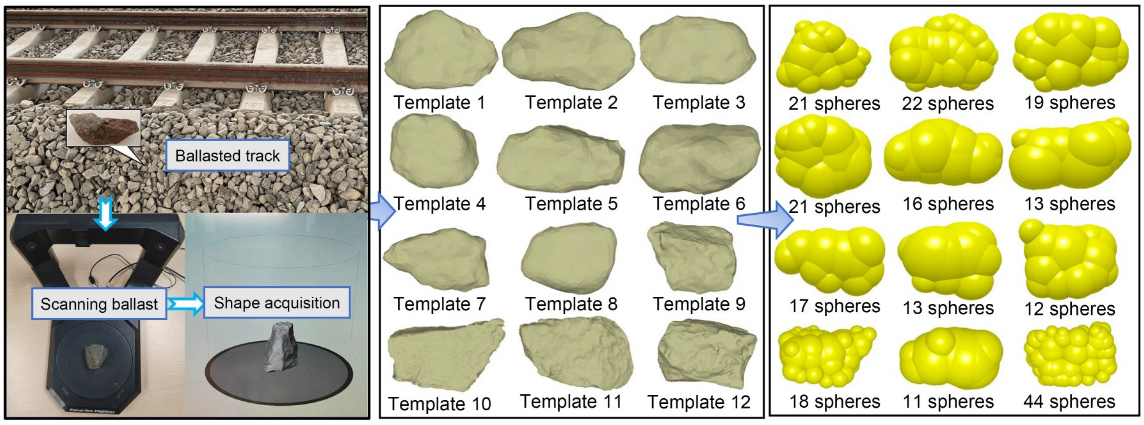

Fig. 1 Modeling process of ballast particles

in multibody dynamics. For example, during a 1.5 s tamping process, sleeper elevation was executed at 0.0–0.1 s, tamper insertion into the ballast bed at 0.1–0.3 s, squeezing stage beneath sleepers at 0.3–0.9 s, and tamper reverse rotation with upward lifting at 0.9–1.5 s (Shi et al., 2020). Throughout the operation, the tamper maintained continuous vibration at 35 Hz.

The key parameters for the simulation were determined based on the required material properties and contact mechanics theory, with specific numerical values as detailed in Table 1. The discrepancy in friction coefficient between ballast–ballast and ballast–sleeper interfaces stems from their distinct contact mechanisms, where irregular geometry in multi-sphere modeled ballast provides primary anti-rotation and anti-sliding resistance, while elevated friction coefficients for smooth sleeper surfaces comprehensively represent the composite resistance generated by mechanical interlocking from concrete roughness at the macro scale.

This study implemented dynamic analysis of the ballast bed–tamping device system using a co-simulation framework integrating the DEM and MBD (Fang et al., 2024; Xiao et al., 2024; Zhang et al., 2025). The discretized modeling and motion computations of ballast particles were implemented via a discrete element platform, while the motion behaviors of the tamping device were governed by a multibody dynamics platform.

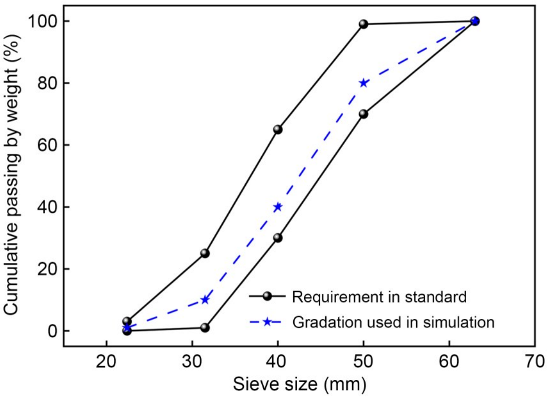

Fig. 2 Ballast gradation

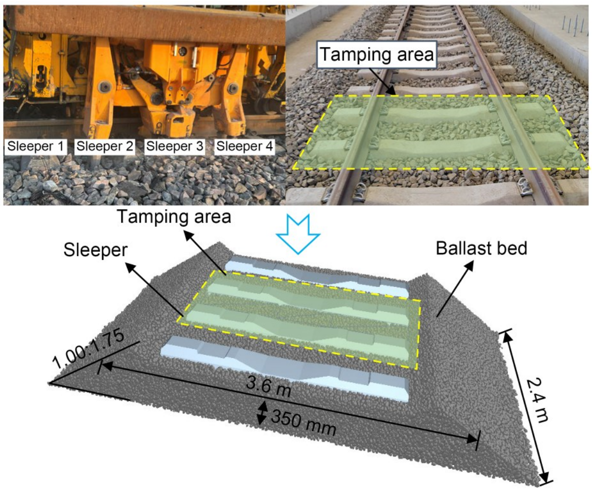

Fig. 3 Simulation model of a ballasted track

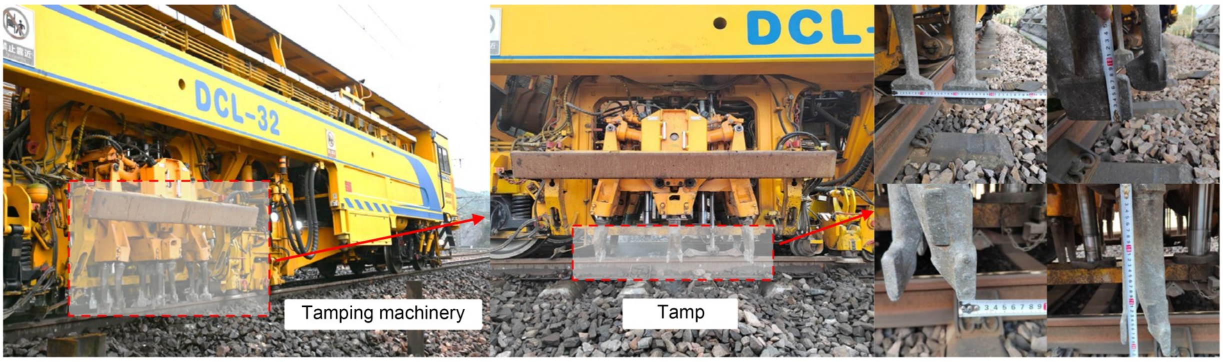

Fig. 4 Dimensions of the tamping device

Table 1 Material parameters

Item	Elastic modulus (GPa)	Poisson's ratio	Density (kg/m^3)	Friction coefficient	Coefficient of restitution
Ballast	59	0.18	2600	0.3	0.5
Sleeper	31	0.20	2500	0.8	0.5
Tamper	207	0.29	7900	0.2	0.5

The contact forces between ballast particles, ballast–sleeper interfaces, and ballast–tamper interactions in discrete element analysis were resolved using the Hertz–Mindlin (no slip) contact model, as detailed in Eqs. (1)–(4) (Qian et al., 2024a) (Fig. 5). In Fig. 5, K_n and C_n represent the normal contact stiffness and damping, respectively, while K_t and C_t denote the tangential contact stiffness and damping, and μ indicates the friction coefficient.

$$F_\text{n}=\frac{4}{3}E^*\sqrt{R^*}\,\alpha^{\frac{3}{2}}-2\sqrt{\frac{5}{6}}\,\beta\sqrt{S_\text{n}m^*}\,v_\text{n}^\text{rel}, \tag{1}$$

$$F_\text{t}=-S_\text{t}\delta-2\sqrt{\frac{5}{6}}\,\beta\sqrt{S_\text{t}m^*}\,v_\text{t}^\text{rel}, \tag{2}$$

where F_n and F_t represent the normal and tangential forces, respectively, E^*, R^*, and m^* denote the equivalent elastic modulus, equivalent radius, and equivalent mass of particles a and b, α is the normal overlap, β relates to the restitution coefficient, δ is the tangential overlap, S_n and S_t are the normal and tangential stiffnesses, respectively, and v_n^rel and v_t^rel correspond to the normal and tangential relative velocities, respectively.

$$S_\text{n}=2E^*\sqrt{R^*\alpha}, \tag{3}$$

$$S_\text{t}=8G^*\sqrt{R^*\alpha}, \tag{4}$$

where G^* represents the equivalent shear modulus between particles. The calculation of contact surface moments for ballast particles (T_i) applies Eq. (5).

$$T_i=-\mu_\text{r}F_\text{n}R_i\boldsymbol{\omega}_i, \tag{5}$$

where μ_r denotes the rolling friction coefficient, R_i represents the distance from the centroid to the contact point, and $\boldsymbol{\omega}_i$ signifies the unit angular velocity vector at the contact point.

The motion equations of ballast particles are derived from Newton's second law, with their acceleration $\ddot{u}_i$ and angular acceleration $\ddot{\theta}_i$ expressed as follows:

$$\sum F=m_i\ddot{u}_i, \tag{6}$$

$$\sum M=I_i\ddot{\theta}_i, \tag{7}$$

where $\sum F$ denotes the resultant force acting on a ballast particle, m_i represents its mass, $\sum M$ signifies the resultant torque on the particle, and I_i indicates its rotational inertia.

Within a single time step, the velocity $\dot{u}_i$ and angular velocity $\dot{\theta}_i$ of ballast particles were solved based on the central difference method, as detailed in Eqs. (8) and (9).

$$(\dot{u}_i)_{N+1/2}=(\dot{u}_i)_{N-1/2}+(\ddot{u}_i)_N\Delta t, \tag{8}$$

$$(\dot{\theta}_i)_{N+1/2}=(\dot{\theta}_i)_{N-1/2}+(\ddot{\theta}_i)_N\Delta t, \tag{9}$$

where $(\dot{u}_i)_{N+1/2}$ represents the velocity at the current time step, $(\dot{u}_i)_{N-1/2}$ denotes the velocity at the previous time step, $(\ddot{u}_i)_N$ signifies the acceleration, Δt indicates the time step size, $(\dot{\theta}_i)_{N+1/2}$ corresponds to the angular velocity at the current time step, $(\dot{\theta}_i)_{N-1/2}$ refers to the angular velocity at the previous time step, and $(\ddot{\theta}_i)_N$ denotes the angular acceleration. The expressions for translational displacement of ballast particles are presented in Eqs. (10) and (11).

$$(u_i)_{N+1}=(u_i)_N+(\dot{u}_i)_{N+1/2}\Delta t, \tag{10}$$

$$(\theta_i)_{N+1}=(\theta_i)_N+(\dot{\theta}_i)_{N+1/2}\Delta t, \tag{11}$$

where $(u_i)_{N+1}$ is the displacement at the next time step, $(u_i)_N$ is the current displacement, $(\theta_i)_{N+1}$ denotes the angular displacement at the next time step, and $(\theta_i)_N$ represents the current angular displacement.

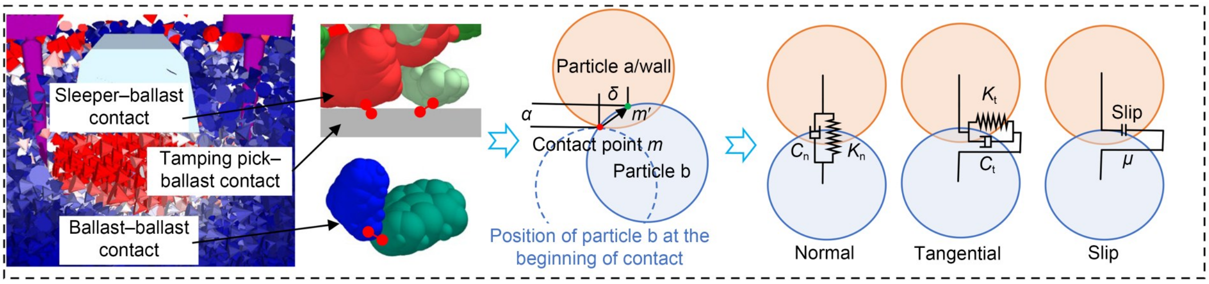

Fig. 5 Contact model

Particle motion data were transmitted to the multibody dynamics domain, where the Lagrange equations were applied to solve the motion equations of the tamping device–sleeper system. Updated rigid-body displacements or velocities were fed back to the discrete element domain via data transfer protocols, driving the regeneration of particle contact states. This cross-platform interaction established a closed-loop coupling mechanism encompassing contact force–motion response–geometric update–contact reconstruction.

2.3 Model verification

The variation in lateral resistance of the ballast bed before and after tamping directly reflects the degree of reconstruction of ballast–sleeper contact states during tamping operations, serving as a critical indicator to quantify model reliability.

A comparative analysis of the sleeper lateral resistance before and after tamping was conducted using the coupling analysis model of the tamping device–ballast bed system established in this study (Fig. 6). Field tests and simulations of lateral resistance in previous studies (Wang et al., 2024) indicate that perturbation of the ballast bed during tamping operations leads to a reduction in lateral resistance. Discrepancies between the results of this study and previous research arise from inevitable variation in the shape and distribution characteristics of ballast particles across different ballast beds. The lateral resistance of the ballast bed before and after tamping maintains fundamental variation trends, with outcomes remaining similar. Fig. 7 illustrates ballast particle movement during lateral resistance testing. A comparison with previous research (Tan et al., 2024) shows similar movement trends, validating the model's reliability.

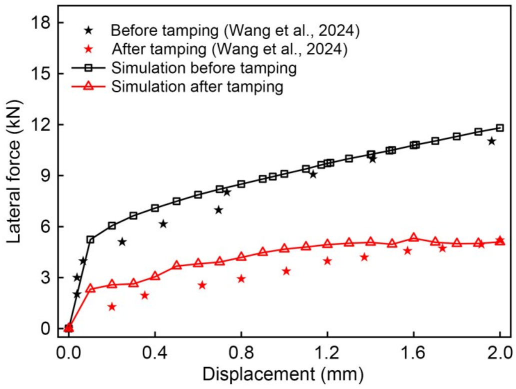

Fig. 6 Comparison of lateral resistance

Tamping operations in railways alter the compactness of the ballast bed, a critical indicator for evaluating tamping quality. This study validated the simulation model using the compactness variation patterns derived from simulation analyses by Zhang et al. (2023a). In Fig. 8, areas A1–A4 correspond to the rail seat support area beneath one side of the sleeper; areas B1–B4 represent the region beneath the sleeper center; areas C1–C4 denote the ballast shoulder area outside the sleeper; areas D1–D6 indicate the tamper inserting area; areas E1–E6 represent the inter-tamper region. The locations for areas A–E are consistent with those of Zhang et al. (2023a). The trends in compactness variation across these areas show consistent regularity and demonstrate close numerical proximity (Fig. 9). Discrepancies in compactness values are acceptable due to significant differences in the initial conditions, including differences in tamping device configurations and ballast bed parameters between the two models. These findings

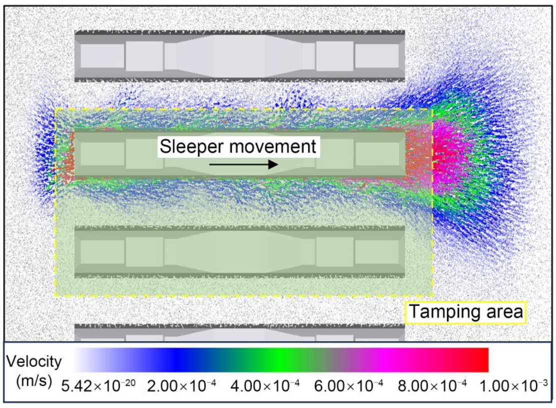

Fig. 7 Ballast movement

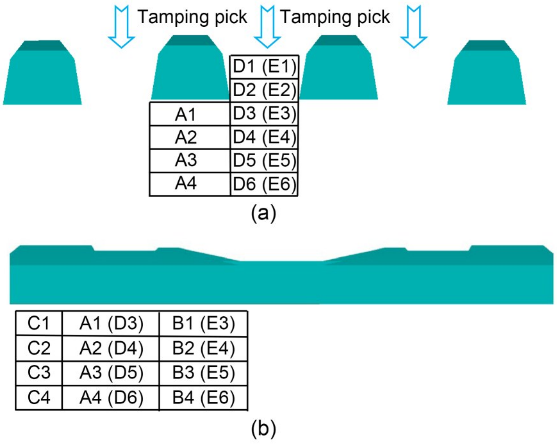

Fig. 8 Ballast bed area division: (a) vertical section; (b) cross section

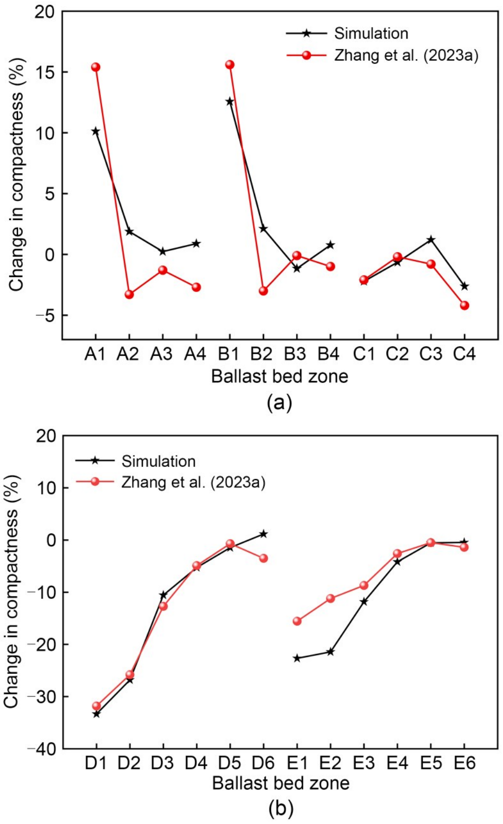

Fig. 9 Compaction comparison: (a) areas A–C; (b) areas D and E

collectively validate the reliability of the analytical model established in this study.

3 Results and discussion

Based on practical engineering operations, in this study, we analyzed the mechanical characteristics of a ballast bed, including internal compactness, kinematic patterns, contact behavior, and mechanical energy, with the tamping duration increasing from 1.0 to 3.0 s. The time proportions of each stage (track lifting, tamper inserting, etc.) during a single tamping operation are shown in Fig. 10. To investigate the differential impact of tamping duration on distinct areas of the ballast bed, different internal areas of the ballast bed were delineated (Fig. 11).

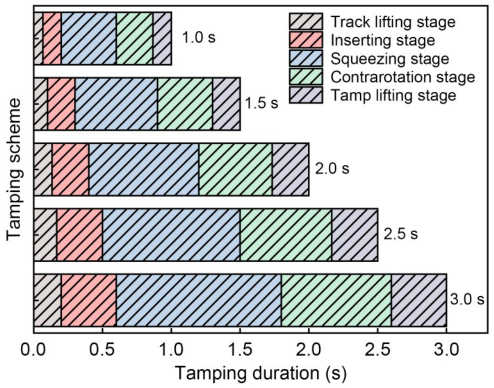

Fig. 10 Time division of each stage of the tamping operation

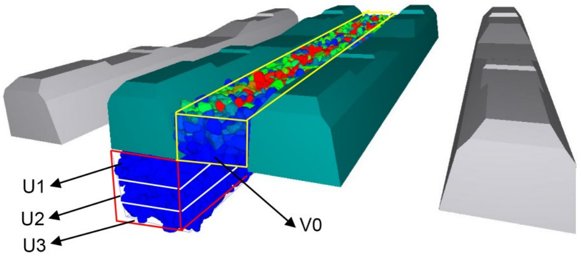

Fig. 11 Statistical areas delineated to investigate the effects of tamping duration

3.1 Change of ballast bed compactness

The main objective of tamping maintenance operations for ballasted tracks is to reduce track irregularities through lifting and aligning procedures, enhance compactness beneath sleepers, and restore the load-bearing capacity of the ballast bed. This study focused on analyzing the effects of tamping on the compactness of the ballast bed, as defined in Eq. (12):

$$D = \frac{m_{\text{ballast}}}{V_{\text{statistical}} \rho_{\text{ballast}}} \times 100\%, \tag{12}$$

where D is the compactness of a specific area, m_{ballast} represents the total mass of ballast in that area, $V_{\text{statistical}}$ denotes the statistical area volume, and ρ_{ballast} indicates the density of the ballast material.

The evolution of ballast bed compactness beneath sleepers and in inter-sleeper regions is shown in Fig. S3 of the ESM. Fig. S3a of the ESM shows that voids beneath sleepers emerge during the track lifting stage. Compaction forces induced by the tamper inserting into the ballast bed force ballast particles to rapidly rearrange and fill these voids, resulting in pronounced compactness variation in the area beneath the sleepers. During the squeezing stage, a dynamic equilibrium among ballast particles develops, resulting in minor fluctuations in the degree of compaction, exhibiting a saturation effect. Variation in compactness under different tamping durations becomes apparent by the end of the inserting stage, with the 1 s duration yielding minimal compaction improvement. During the contrarotation of the tamper and the tamp lifting stage, the compactness in the ballast bed remains stable under different operation durations.

As the U2 and U3 areas beneath sleepers are not direct tamping zones, the compaction efficiency diminishes with depth. Consequently, the compaction degree changes shown in Figs. S3b and S3c of the ESM are relatively minor compared to those in the U1 area. During the inserting stage, the compaction degree temporarily declines due to disturbance, while vibrational effects during the squeezing stage and contrarotation of the tamper facilitate particle reorientation, gradually restoring compaction. Similarly, this process is influenced by the tamping duration.

The evolution of compactness in the inter-sleeper region of the ballast bed (Fig. S3d of the ESM) showed the most pronounced variation. Direct disturbance caused by tamper insertion leads to an initial decline in compaction. As the compaction process progresses, this area exhibits a gradual reduction or stabilization during the squeezing stage, followed by a partial recovery during the tamper contrarotation phase. However, compaction decreases again during the tamp lifting stage due to partial particle removal from the ballast bed as the tamper withdraws.

The variation in compactness within the ballast bed before and after tamping under different durations is shown in Fig. 12. For the U1 area directly beneath sleepers, the compactness increased by 7.4% under a 1 s tamping duration and 10.8% at 3 s. In the underlying U2 area, the compactness transitioned from reduction to gradual enhancement, while the U3 area showed progressive improvement. This demonstrates that extended single tamping durations enhance compactness beneath sleepers, with diminishing effects at greater depths.

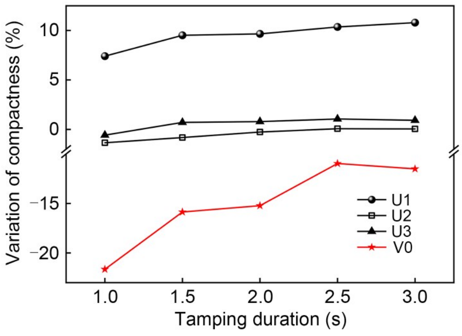

Fig. 12 Variation in compactness of the ballast bed

For the inter-sleeper region, the compactness decreased by 21.6% under a 1 s tamping duration and 11.5% under 3 s, with the reduction magnitude diminishing by 10.1 percentage points. The compactness in this area gradually increased with extended tamping durations. The compactness variation in regions beneath sleepers and inter-sleeper regions shows similar trends, though the ballast bed model mass remained unchanged. Fig. 13 demonstrates that tamping in practical engineering induces destructive phenomena, including ballast particle ejection and accumulation outside the ballast bed. A comparative analysis of compactness variation under different tamping durations in Fig. 12 indicates that shorter tamping durations increase the probability of ballast particle ejection from the ballast bed, resulting in greater damage to bed integrity and representing comparatively adverse effects. Considering the change in uniformity of compactness across the ballast bed, a tamping duration of 2.5 s is recommended to balance operational efficiency and compaction homogeneity.

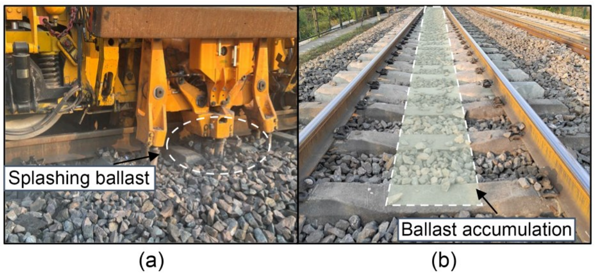

Fig. 13 Influence of tamping on the movement of ballast: (a) during the tamping process; (b) after tamping

3.2 Change of ballast movement

The core objective of tamping operations is to enhance compactness beneath sleepers and the structural stability of the ballast bed by mechanically vibrating ballast particles to migrate beneath the sleepers, filling voids generated during track lifting. In this section, we describe the evolution patterns of ballast particle velocities within the ballast bed under various tamping durations.

Fig. 14a shows the average velocity patterns of ballast particles in area U1 beneath sleepers during different tamping stages. As shown in Fig. 14a, the ballast particle velocity remains unaffected during the sleeper-lifting stage but sharply increases to a peak value under tamper action in the inserting stage, subsequently

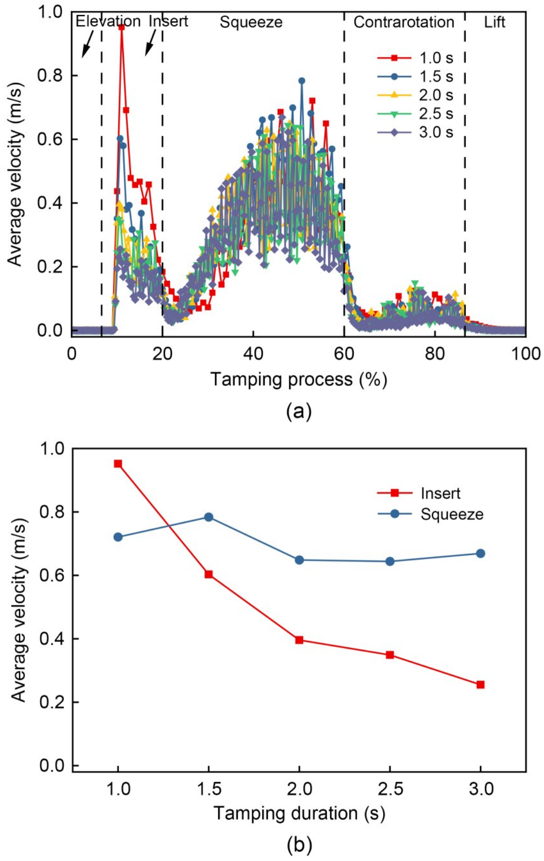

(a)

(b)

Fig. 14 Ballast velocity beneath a sleeper: (a) time history curve; (b) characteristic value

decreasing, indicating a significant effect of tamping operations on the inserting stage. During the squeezing stage, continuous oscillation of the tamper and its gradual proximity to ballast particles beneath sleepers induce an oscillatory upward trend in velocity. A slight vibration occurs during tamper contrarotation withdrawal, while the velocity approaches 0 m/s in the tamp lifting stage. The highest velocities emerge in the inserting and squeezing stages, therefore, the maximum average velocities within these phases were selected as characteristic values for analysis.

Fig. 14b shows the evolution of characteristic velocity values during the inserting and squeezing stages. At a tamping duration of 1 s, the peak velocity in the inserting stage reaches 0.95 m/s, then sequentially decreases to 0.60, 0.40, 0.35, and finally 0.26 m/s at 3 s, an overall reduction of 72.6%. This stage shows a pronounced effect of tamping duration on ballast particle velocity. In the squeezing stage, the maximum velocity decreases from 0.72 m/s at 1 s to 0.67 m/s at 3 s, a gradual overall decline of 7%, indicating a slow attenuation trend of particle velocity with prolonged tamping durations.

The pattern of variation in velocity in the inter-sleeper region under tamper insertion is shown in Fig. 15. Fig. 15a presents average velocity–stage curves under various tamping durations. The velocity profile during the inserting stage aligns with the ballast motion beneath sleepers shown in Fig. 14a, exhibiting rapid acceleration followed by deceleration under tamper action. However, during the squeezing stage and tamper contrarotation phase, unlike in the area beneath the sleeper, the ballast velocity maintains relative stability. The vibration effect of the tamper has limited influence in this area. Shorter tamping durations correlate with higher velocity during the stabilized phase. The tamp lifting stage shows upward velocity amplification within the ballast bed due to vertical tamper retraction. Pronounced terminal velocity increments in both the inserting and lifting stages justify adopting maximum mean velocity across these phases as the characteristic parameter for inter-sleeper region analysis.

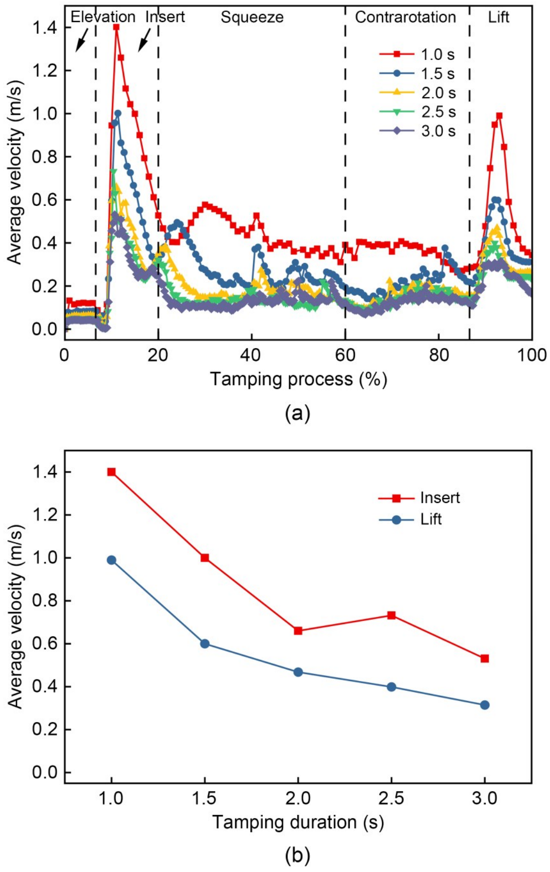

(a)

(b)

Fig. 15 Ballast velocity in the inter-sleeper region: (a) time history curve; (b) characteristic value

The velocity in the inserting stage decreases from a maximum of 1.40 m/s at 1 s tamping duration to 0.53 m/s at 3 s, a reduction of 62% (Fig. 15b). Similarly, during the tamp lifting stage, the velocity declines from 0.99 to 0.31 m/s, representing a 69% reduction. The inter-sleeper region shows significantly greater susceptibility to tamping duration across all operational stages than the area beneath the sleepers.

The spatial evolution of ballast velocity is shown in Fig. S4 of the ESM. Notably, values such as 0.11 s at 1.0 s of tamping duration and 0.33 s at 3.0 s of tamping duration represent identical tamping progress under different tamping durations. During the inserting stage, ballast movement radiates from the lowermost part of the tamper under impact, with shorter tamping durations inducing greater particle displacement along both depth and longitudinal directions, concurrently exhibiting tendencies for migration toward the area beneath the sleepers. In the squeezing stage, particle motion is concentrated mainly beneath the sleepers, dominated by longitudinal displacement. The tamp lifting stage showed the most significant effect on the inter-sleeper region, where ballast particles migrated upward through the ballast bed, with this trend being more pronounced under shorter operational durations.

The ballast movement during tamping encompasses both translational and rotational motion. The intensity of interparticle collisions during compaction can be assessed by analyzing the rotational velocity of ballast particles. The evolution of angular velocity in ballast particles beneath sleepers under different tamping durations is shown in Fig. 16. Fig. 16a shows that ballast rotation beneath sleepers exhibits a maximum response during the inserting and squeezing stages, with persistent oscillations observed in the squeezing stage and weaker oscillations during the contrarotation phase of tamping. Fig. 16b shows a significant reduction in peak angular velocity during the inserting stage as the tamping duration increases, decreasing from 11.7 rad/s at 1 s to 4.5 rad/s at 3 s, a 61.5% reduction, while values in the squeezing stage decline from 8.7 to 7.5 rad/s.

The patterns of variation in average angular velocity in the inter-sleeper region are shown in Fig. 17a. A comparison with Fig. 15 shows similar evolution trends between ballast particle velocities and angular velocities, particularly in showing the maximum response during the inserting stage and a significant effect during the tamp lifting stage. Fig. 17b reveals a continuous angular velocity reduction with increasing tamping duration, decreasing from 33.1 rad/s at 1 s to 13.9 rad/s at 3 s in the inserting stage and from 16.8 rad/s at 1 s to 8.2 rad/s at 3 s in the lifting stage. Comparisons of Figs. 14 and 16 and Figs. 15 and 17 show more pronounced particle motion in the inter-sleeper region than beneath the sleepers, evident in both the velocity and angular velocity parameters.

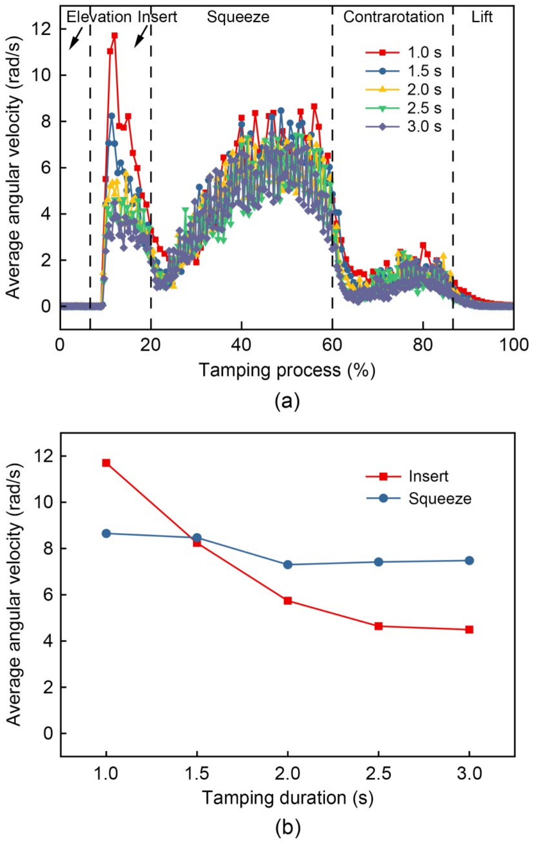

(a)

(b)

Fig. 16 Ballast angular velocity beneath a sleeper: (a) time history curve; (b) characteristic value

The spatial evolution of angular velocity in ballast particles across different tamping stages is shown in Fig. S5 of the ESM and shows trends similar to those of the translational motion patterns in Fig. S4 of the ESM. During the inserting stage, a diffusion pattern can be seen centered around the tamper's lowest end. The squeezing stage concentrates mainly rotational motion beneath the sleepers with dominant longitudinal rotation. The tamp lifting stage reveals a tendency toward rotation extending to the outer ballast bed. Prolonged tamping duration corresponds to a smaller affected area within the same operational stage.

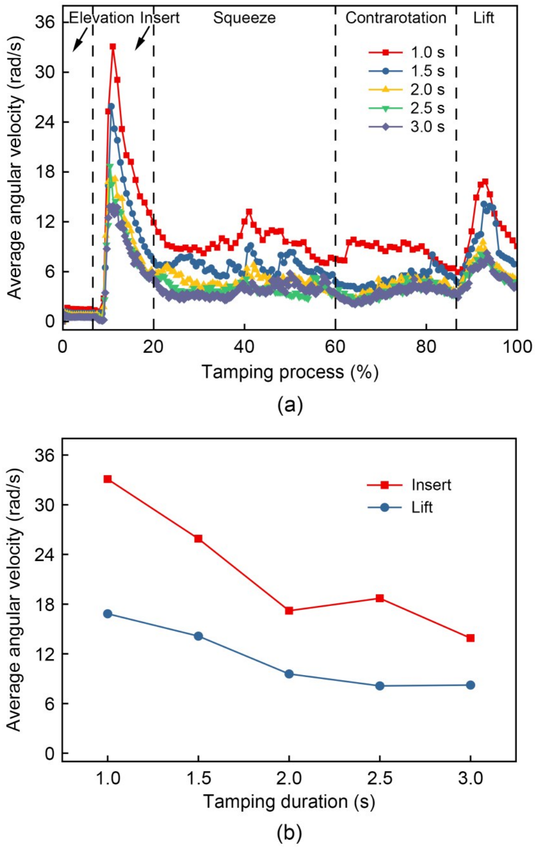

Fig. 17 Ballast angular velocity in the inter-sleeper region: (a) time history curve; (b) characteristic value

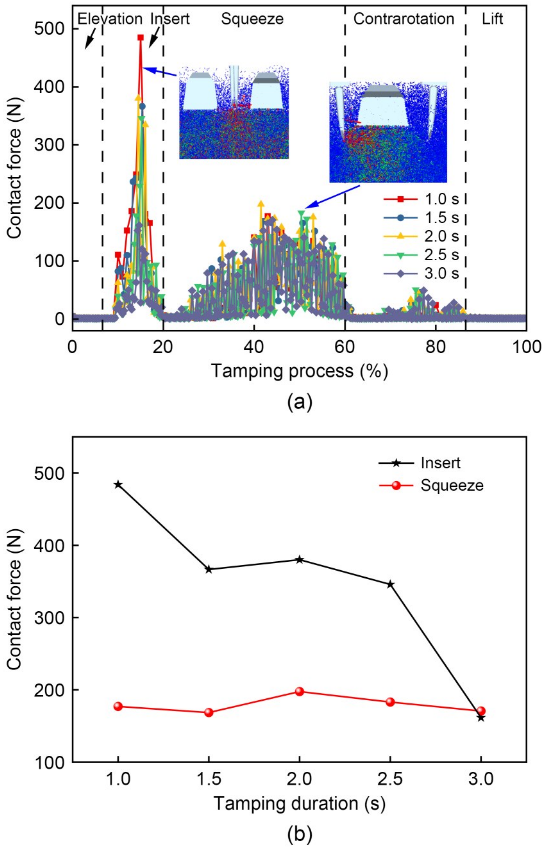

Fig. 18 Normal contact force of ballast beneath a sleeper: (a) time history curve; (b) characteristic value

3.3 Influence on ballast contact

The intense collision contacts between tampers and ballast particles during tamping operations may induce particle pulverization and fracture, potentially compromising normal track structural performance. To optimize tamping durations, analysis of interparticle contact behavior under various operational times requires systematic investigation.

Fig. 18 shows the patterns of variation of normal contact forces in the area beneath sleepers. As revealed in Fig. 18a, the contact force shows a notable increase followed by attenuation during the inserting stage. During the squeezing stage, the contact force shows an oscillatory trend of gradual amplification followed by reduction. The maximum value of average contact forces from both the inserting and squeezing stages was selected as the characteristic value. Fig. 18b indicates that the normal contact forces during the inserting stage significantly exceed those in the squeezing stage. At a 1 s tamping duration, the characteristic value of normal contact force during the inserting stage measures 484 N, which decreases by 66.7% to 161 N at a 3 s tamping duration, exhibiting the most significant reduction influenced by the tamping duration. In contrast, the characteristic values during the squeezing stage remain relatively stable, showing less sensitivity to tamping duration variations.

As shown in Figs. 18a and 19a, both the normal and tangential contact forces in the ballast bed show consistent variation patterns, with significant decreases in contact forces during the inserting stage as the tamping duration increases. This phenomenon indicates that appropriately extending the tamping duration optimizes the contact force distribution within the ballast bed and reduces the probability of ballast breakage.

Fig. S6 of the ESM depicts the normal contact force distributions in the ballast bed during both the inserting and squeezing stages. Upon initial tamper-ballast contact, pronounced force variations emerge in the inter-sleeper region, propagating radially from the tamper's lowest extremity into the deeper ballast layers. Shorter tamping durations intensify this force

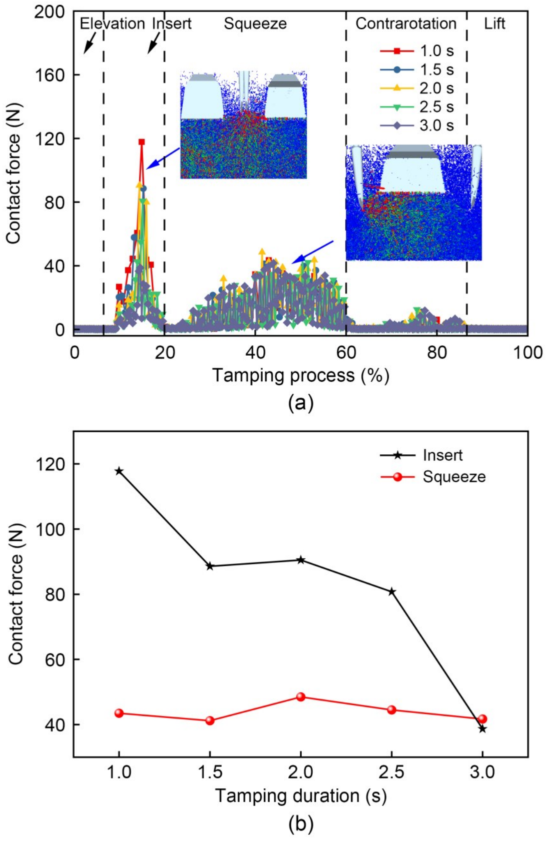

(a)

(b)

Fig. 19 Tangential contact force of ballast beneath a sleeper: (a) time history curve; (b) characteristic value

propagation phenomenon. During squeezing operations, tampers compress the area beneath sleepers, generating fan shaped distribution patterns aligned with tamper deflection orientations. The extent of the spatial effect of contact forces remains consistent across different tamping durations in squeezing operations.

The particle coordination number, serving as a critical indicator for evaluating ballast rearrangement effectiveness, quantifies the contact between a ballast particle and its adjacent counterparts, thereby assessing interparticle support stability. The calculation of the average coordination number $\overline{C_{\mathrm{N}}}$ is expressed by Eq. (13) (Zhang et al., 2023b).

$$\overline{C_{\mathrm{N}}}=\frac{2N_{\mathrm{C}}}{N_{\mathrm{P}}}, \tag{13}$$

where N_{C} is counted as the total number of distinct contact pairs in the system and N_{P} represents the total particle count in the system.

Variation in the coordination number directly reflects the dynamic restructuring of contact networks among ballast particles during tamping. Fig. 20 shows that during the elevation stage, the abrupt disturbance of ballast beneath sleepers caused by sleeper elevation induces a slight decrease in coordination number. In the inserting stage, forced intrusion of tampers disrupts the original force equilibrium between particles, leading to fractured contacts and loosened ballast beds. This is evidenced by a sharp drop in coordination number, indicating an instantaneous loss of stability and a transition from compacted to disordered states. Throughout the squeezing stage, persistent tamper vibration drives microscale slippage and local rearrangement of particles, with continuous oscillations in coordination number. This demonstrates a dynamic equilibrium between energy input and frictional dissipation where some particles establish new contacts through vibration induced kinetic energy while highly energized particles detach from existing contacts, forming a dynamically stable critical state. During the tamp lifting stage, tamper withdrawal eliminates external forces, allowing gravitational settling where adjacent particles fill voids and progressively raising the coordination number as particles self-organize into more stable structures, enhancing ballast bed stiffness. Notably, increased tamping duration augments vibrational energy input, facilitating optimal repositioning of additional particles, elevating the coordination number from 5.45 to 5.96. This enhancement strengthens force chain transmission efficiency while dispersing sleeper loads through increased contact points, significantly mitigating long term settlement deformation.

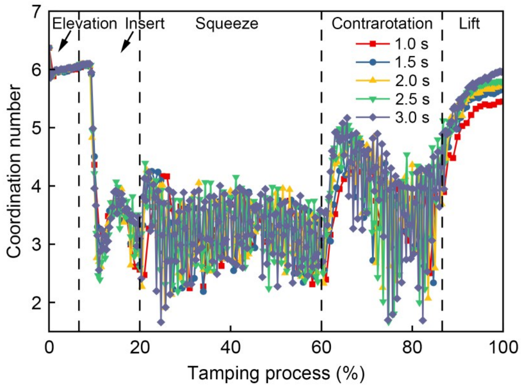

Fig. 20 Average coordination number of ballast

3.4 Influence on the evolution of energy

The analysis of mechanical energy evolution during tamping operations reveals vibration energy transmission in granular systems, elucidating dynamic correlations between structural rearrangement and stabilization in ballast beds. The translational kinetic energy K_i, rotational kinetic energy M_i, potential energy P_i, and mechanical energy E of the ballast particles shown in Fig. S7 of the ESM were calculated according to the methods described by Chi et al. (2024b) and Qian et al. (2024b), as detailed in Eqs. (14)–(17).

$$K_i=\sum\frac{1}{2}m_i v_i^2, \tag{14}$$

$$M_i=\sum\frac{1}{2}I_i\omega_i^2, \tag{15}$$

$$P_i=\sum m_i g h_i, \tag{16}$$

$$E=K_i+M_i+P_i, \tag{17}$$

where v_i is the velocity of the particle, ω_i is the angular velocity of the particle, h_i is the vertical distance of a ballast particle from the zero-potential reference plane, and g is the acceleration of gravity.

Fig. S7 of the ESM shows the variation in the mechanical energy of ballast particles in the area beneath sleepers under different tamping durations. The translational kinetic energy pattern shown in Fig. S7a of the ESM shows that the energy variation during the squeezing stage exceeds that of the inserting stage with prolonged tamping duration. Similar trends are observed for rotational kinetic energy (Fig. S7b of the ESM). Comparative analysis reveals strong correlations between the evolution of translational/rotational kinetic energies and ballast particle motion patterns, as described in Section 3.2. The potential energy change shown in Fig. S7c of the ESM exhibits a substantial dependence on compactness evolution, with increasing potential energy increments as tamping duration extends. Comparisons of mechanical energy in ballast particles shown in Fig. S7d of the ESM show that potential energy exerts the predominant effect on mechanical energy. The extended tamping duration corresponds to increased energy input into the ballast bed.

3.5 Effect of tamping duration on the ballast bed state after tamping

To comprehensively analyze the impact of tamping duration, Fig. S8 of the ESM illustrates the evolution of ballast bed resistance post-tamping while Fig. S9 of the ESM shows the deformation behavior of ballast bed support stiffness. Data trends in Fig. S8 of the ESM indicate progressively increasing ballast bed resistance with extended tamping duration, showing a 56.8% enhancement in lateral resistance when duration increases from 1 to 3 s. Similarly, analysis of support stiffness in Fig. S9 of the ESM reveals a 1.46-fold increase, indicating that prolonged tamper action provides more sufficient particle rearrangement and densification processes, thereby improving the overall structural integrity and collaborative load-bearing capacity of the ballast bed, which macroscopically manifests as growth in lateral resistance and support stiffness.

To analyze the long-term mechanical performance of the ballast bed after tamping, we conducted simulation analysis under cyclic train loading on ballast bed states affected by different tamping durations, with reference to existing research methodologies (Gao et al., 2014; Chen et al., 2025), yielding the settlement deformation results shown in Fig. 21. Combined analysis of post-tamping ballast bed resistance and vertical stiffness shows that an extended tamping duration enhances the bed's deformation resistance capacity, indicating the benefit of appropriately prolonging the tamping time.

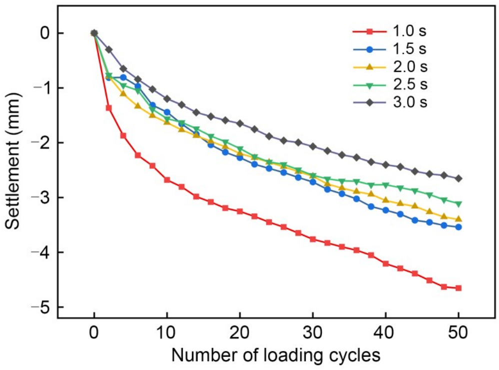

Fig. 21 Effect of different tamping durations on ballast bed settlement

4 Conclusions

In this study, we systematically investigated the correlation between tamping duration parameters of large tamping machinery and dynamic responses in ballasted track structures through a DEM−MBD coupling model integrating tamping mechanisms and the ballast bed. The main conclusions are as follows:

(1) The variation in tamping duration significantly affects ballast particle velocities. During the inserting

stage, prolonging the tamping duration from 1 to 3 s results in a 72.6% reduction in the velocity of ballast particles beneath sleepers and a 62% decrease in the inter-sleeper region. The squeezing stage shows a gradual 7% velocity decline beneath sleepers, while the tamp lifting stage exhibits a 69% velocity reduction in the inter-sleeper region. The inter-sleeper region shows the highest sensitivity to tamping duration. Angular velocity evolution patterns in the ballast bed align closely with velocity changes.

(2) The patterns of evolution of translational and rotational kinetic energy in ballast particles are closely correlated with their motion characteristics. Mechanical energy exhibits the most significant oscillatory variations in the squeezing stage.

(3) Prolonged tamping duration significantly reduces contact forces in ballast particles during the inserting stage while remaining minimally affected in the squeezing stage. The coordination number of ballast particles shows a positive correlation with the tamping duration.

(4) Increased tamping duration enhances ballast bed compactness, improves uniformity in compactness distribution, and increases post-tamping resistance, support stiffness, and long-term deformation resistance capacity.

Acknowledgments

This work is supported by the National Key Research and Development Program of China (No. 2023YFB2604304), the Fundamental Research Funds for the Central Universities (No. 2024YJS042), the 111 Project (No. B20040), and the Science Technology Research and Development Program of China Academy of Railway Sciences Co., Ltd. (No. 2023YJ303).

Author contributions

Tao XIN designed the research. Chao KONG, Zhongxia QIAN, Yi YANG, and Chuanqing DAI processed the corresponding data. Chao KONG wrote the first draft of the manuscript. Yanhua LI helped to organize the manuscript. Sen WANG revised and edited the final version.

Conflict of interest

Chao KONG, Tao XIN, Zhongxia QIAN, Yi YANG, Chuanqing DAI, Yanhua LI, and Sen WANG declare that they have no conflict of interest.

References

Abbasi A, Zakeri JA, Norouzi E, et al., 2024. Field investigation on the effect of the tamping machine and dynamic track stabilizer on changing the rail support modulus. *Proceedings of the Institution of Mechanical Engineers, Part F: Journal of Rail and Rapid Transit*, 238(9):1072-1083.
https://doi.org/10.1177/09544097241255718

Aela P, Zong L, Esmaeili M, et al., 2022. Angle of repose in the numerical modeling of ballast particles focusing on particle-dependent specifications: parametric study. *Particuology*, 65:39-50.
https://doi.org/10.1016/j.partic.2021.06.006

Aingaran S, Le Pen L, Zervos A, et al., 2018. Modelling the effects of trafficking and tamping on scaled railway ballast in triaxial tests. *Transportation Geotechnics*, 15:84-90.
https://doi.org/10.1016/j.trgeo.2018.04.004

Barbir O, Adam D, Kopf F, et al., 2018. Development of condition-based tamping process in railway engineering. *CE/Papers*, 2(2-3):969-974.
https://doi.org/10.1002/cepa.797

Chen C, Li PY, McDowell G, et al., 2025. Numerical study on ballast disturbance and maintenance performance of tamping and stone-blowing. *Construction and Building Materials*, 460:139837.
https://doi.org/10.1016/j.conbuildmat.2024.139837

Chi YH, Xiao H, Zhang ZH, et al., 2022. Discrete element analysis on mechanical properties of ballast bed by tamping in railway turnout areas. *Journal of Computational and Nonlinear Dynamics*, 17(11):111005.
https://doi.org/10.1115/1.4055429

Chi YH, Xiao H, Zhang ZH, et al., 2024a. Analysis of the influence of vibration frequency and amplitude on ballast bed tamping operation in railway turnout areas. *Computational Particle Mechanics*, 11(2):771-788.
https://doi.org/10.1007/s40571-023-00652-4

Chi YH, Xiao H, Zhang ZH, et al., 2024b. Investigating the impact of tamping on ballast bed in railway turnout areas: insights from discrete element method analysis of energy evolution. *Transportation Geotechnics*, 46:101243.
https://doi.org/10.1016/j.trgeo.2024.101243

Cui XH, Xiao H, Xu Y, et al., 2024. Discrete element analysis of the dynamic behavior of ballast track-subgrade system under train dynamic load. *Soil Dynamics and Earthquake Engineering*, 183:108820.
https://doi.org/10.1016/j.soildyn.2024.108820

Fang J, Zhao CF, Cai CS, et al., 2024. Mechanical behavior and performance evolution of railway ballast track under dynamic stabiliser based on the hybrid MBD–DEM simulation. *Transportation Geotechnics*, 46:101264.
https://doi.org/10.1016/j.trgeo.2024.101264

Gao L, Luo Q, Xu Y, et al., 2014. Railway ballast bed mechanical property based on discrete element method. *Journal of Tongji University (Natural Science)*, 42(7):1064-1069 (in Chinese).
https://doi.org/10.3969/j.issn.0253-374x.2014.07.012

Gao L, Shi SW, Zhong YL, et al., 2023. Real-time evaluation of mechanical qualities of ballast bed in railway tamping maintenance. *International Journal of Mechanical Sciences*, 248:108192.
https://doi.org/10.1016/j.ijmecsci.2023.108192

Gao L, Shi SW, Cai XP, et al., 2024. Research on interaction of tamping machine-ballast bed and influence of tamping frequency. *Engineering Mechanics*, 41(12):30-41 (in Chinese).
https://doi.org/10.6052/j.issn.1000-4750.2022.09.0828

Gu QS, Zhao C, Bian XC, et al., 2022. Trackbed settlement and associated ballast degradation due to repeated train moving loads. *Soil Dynamics and Earthquake Engineering*, 153:107109.
https://doi.org/10.1016/j.soildyn.2021.107109

Guo YL, Markine V, Jing GQ, 2021. Review of ballast track tamping: mechanism, challenges and solutions. *Construction and Building Materials*, 300:123940.
https://doi.org/10.1016/j.conbuildmat.2021.123940

Indraratna B, 2016. 1st Proctor Lecture of ISSMGE: railroad performance with special reference to ballast and substructure characteristics. *Transportation Geotechnics*, 7:74-114.
https://doi.org/10.1016/j.trgeo.2016.05.002

Kumara JJ, Hayano K, 2016. Deformation characteristics of fresh and fouled ballasts subjected to tamping maintenance. *Soils and Foundations*, 56(4):652-663.
https://doi.org/10.1016/j.sandf.2016.07.006

Lim WL, McDowell GR, 2005. Discrete element modelling of railway ballast. *Granular Matter*, 7(1):19-29.
https://doi.org/10.1007/s10035-004-0189-3

Liu JX, Wang P, Liu GZ, et al., 2020. Influence of a tamping operation on the vibrational characteristics and resistance-evolution law of a ballast bed. *Construction and Building Materials*, 239:117879.
https://doi.org/10.1016/j.conbuildmat.2019.117879

MOR (Ministry of Railways of the People's Republic of China), 2008. Railway Ballast, TB/T 2140-2008. National Standards of the People's Republic of China (in Chinese).

NRA (National Railway Administration of the People's Republic of China), 2017. Code for Design of Railway Track, TB 10082-2017. National Standards of the People's Republic of China (in Chinese).

Offenbacher S, Antony B, Barbir O, et al., 2021. Evaluating the applicability of multi-sensor equipped tamping machines for ballast condition monitoring. *Measurement*, 172:108881.
https://doi.org/10.1016/j.measurement.2020.108881

Przybyłowicz M, Sysyn M, Gerber U, et al., 2022. Comparison of the effects and efficiency of vertical and side tamping methods for ballasted railway tracks. *Construction and Building Materials*, 314:125708.
https://doi.org/10.1016/j.conbuildmat.2021.125708

Qian Y, Tutumluer E, Hashash YMA, et al., 2022. Triaxial testing of new and degraded ballast under dry and wet conditions. *Transportation Geotechnics*, 34:100744.
https://doi.org/10.1016/j.trgeo.2022.100744

Qian ZX, Xiao H, Kong C, et al., 2024a. Discrete element analysis of the dynamic mechanical characteristics of ballasted track on bridges under train loading. *International Journal of Structural Stability and Dynamics*, 26(5):2650023.
https://doi.org/10.1142/S0219455426500239

Qian ZX, Xiao H, Feng RL, et al., 2024b. Mechanism of manual tamping operation for ballast bed based on DEM–MBD coupling. *Computational Particle Mechanics*, 11(4):1627-1640.
https://doi.org/10.1007/s40571-023-00689-5

Shi SW, Gao L, Cai XP, et al., 2020. Effect of tamping operation on mechanical qualities of ballast bed based on DEM–MBD coupling method. *Computers and Geotechnics*, 124:103574.
https://doi.org/10.1016/j.compgeo.2020.103574

Shi SW, Gao L, Xiao H, et al., 2021. Research on ballast breakage under tamping operation based on DEM–MBD coupling approach. *Construction and Building Materials*, 272:121810.
https://doi.org/10.1016/j.conbuildmat.2020.121810

Shi SW, Wang J, Gao L, et al., 2024. Intelligent optimization of tamping parameters using discrete element and radial basis function–multi-objective genetic algorithm (RBF–MOGA). *Automation in Construction*, 168:105752.
https://doi.org/10.1016/j.autcon.2024.105752

Tan P, Xiao YJ, Jiang Y, et al., 2024. Investigating influencing mechanisms of under-sleeper pads on lateral resistance of ballasted railway trackbed via hybrid DEM–FDM simulations. *Transportation Geotechnics*, 45:101200.
https://doi.org/10.1016/j.trgeo.2024.101200

Wang CY, Shi SW, Gao L, et al., 2024. Influence of consecutive tamping operations on failures of ballast bed and tamping machine. *Engineering Failure Analysis*, 163:108583.
https://doi.org/10.1016/j.engfailanal.2024.108583

Wang M, Xiao YJ, Li WQ, et al., 2022. Characterizing particle-scale acceleration of mud-pumping ballast bed of heavy-haul railway subjected to maintenance operations. *Sensors*, 22(16):6177.
https://doi.org/10.3390/s22166177

Xiao H, Zhang ZH, Zhu YJ, et al., 2023. Experimental analysis of ballast bed state in newly constructed railways after tamping and stabilizing operation. *Construction and Building Materials*, 362:129772.
https://doi.org/10.1016/j.conbuildmat.2022.129772

Xiao H, Chi YH, Zhang ZH, et al., 2024. Study on the splashing behavior of high-speed railway ballast in ice and snow environment: analysis of the influence of the train speed, ice mass and striking position. *Construction and Building Materials*, 411:134383.
https://doi.org/10.1016/j.conbuildmat.2023.134383

Xu Y, Yu WY, Qie L, et al., 2021. Analysis of influence of ballast shape on abrasion resistance using discrete element method. *Construction and Building Materials*, 273:121708.
https://doi.org/10.1016/j.conbuildmat.2020.121708

Zhang X, Zhao CF, Zhai WM, 2019. Importance of load frequency in applying cyclic loads to investigate ballast deformation under high-speed train loads. *Soil Dynamics and Earthquake Engineering*, 120:28-38.
https://doi.org/10.1016/j.soildyn.2019.01.023

Zhang ZH, Xiao H, Zhu YJ, et al., 2023a. Macro-meso mechanical properties of ballast bed during three-sleeper tamping operation. *International Journal of Rail Transportation*, 11(6):886-911.
https://doi.org/10.1080/23248378.2022.2129493

Zhang ZH, Xiao H, Wang Y, et al., 2023b. Numerical simulation of the three-sleeper asynchronous tamping operation of ballast bed based on the virtual unit module and polyhedral ballast model. *Transportation Geotechnics*, 40: 100964.
https://doi.org/10.1016/j.trgeo.2023.100964

Zhang ZH, Xiao H, Gan TC, et al., 2024. Experimental study on vibration transmission and attenuation characteristics of ballasted track under excitation of three-sleeper tamping machine. *Journal of the China Railway Society*, 46(3): 21-31 (in Chinese).
https://doi.org/10.3969/j.issn.1001-8360.2024.03.003

Zhang ZH, Xiao H, Ma CZ, et al., 2025. Vibration characteristics and mesoscopic state evolution of ballasted track during dynamic stabilizing operation. *International Journal of Structural Stability and Dynamics*, 25(15):2550157.
https://doi.org/10.1142/S0219455425501573

Zhou TY, Hu B, Sun JF, et al., 2013. Discrete element method simulation of railway ballast compactness during tamping process. *The Open Electrical & Electronic Engineering Journal*, 7(1):103-109.
https://doi.org/10.2174/1874129001307010103

Zhou YL, Schlake B, Hansmann F, et al., 2024. Particle motion and stress response interacted with machine activity: railroad tamping strategy. *Transportation Geotechnics*, 45: 101188.
https://doi.org/10.1016/j.trgeo.2024.101188

Electronic supplementary materials

Figs. S1–S9, Table S1